Torque ripple minimization in Consequent-Pole PM Machines using harmonic current injection

Samad Taghipour Boroujeni*, Seyed Payam Emami, Noureddine Takorabet, and Amin Mahmoudi

***Abstract*— In this paper, the torque ripple of consequent-pole PM machines (CPPMMs) is reduced by injecting 2nd order harmonic of the armature current. In the proposed method, based on the machine back-emf spectrum and the current main harmonic, appropriate 2nd order harmonic of the armature current is obtained. An analytical model is developed to obtain back-emf of CPPMMs. In addition, the obtained analytical model is used to compute the developed electromagnetic torque as a function of the armature currents. Validity of the analytical model is verified using finite-element analysis. To investigate the efficacy of the proposed 2nd order current harmonic in torque ripple minimization, the optimum one is obtained separately by a direct search algorithm and the related electromagnetic torque waveforms for two different obtained 2nd order current harmonics are compared together. The developed analytical model is used in the direct search algorithm for the torque waveform computation. Although the proposed method is not as exact as the direct search method, it is precise enough considering its negligible computation burden over the direct search method.**

***Index Terms*— Analytical model, consequent-pole PM machine, harmonic injection, torque ripple reduction.**

I. Introduction

Due to the merits of PM machines such as high torque density and easiness of their control, they are interesting actuators to be used in many industrial and domestic applications. The main disadvantage of the PM machines is their high torque ripple. The torque ripple in PM machines includes two main sources, i.e., cogging torque and pulsating electromagnetic torque. Cogging torque is generated due to the tendency of the PMs to be aligned with the stator ferromagnetic teeth, and the pulsating electromagnetic torque is the result of interaction of the PM field and the armature current.

There are some techniques for reducing cogging torque of PM machines such as PM shaping [1], PM segmentation [2,3], PM shifting [4] and skewing [5]. Choosing an appropriate combination of the stator slot and rotor pole numbers is the most effective method in cogging torque reduction [6]. Due to a very small value of the greatest common multiplier of pole and stator teeth numbers in fractional slot PM machines, their cogging torque is too small [6]. However, due to the concentrated winding of fractional slot machines, there is a considerable harmonic content of the armature flux density, and this results in a high level of pulsating torque in the fractional slot PM machines [7,8]. In comparison with surface-mounted PM machines, consequent-pole PM machines (CPPMMs) have lower cogging torque [9], because, one-half of the machine PM poles are replaced by ferromagnetic iron poles. The other merits of CPPMMs are lower PM usage [9], lower eddy currents in the PM blocks [10], and higher flux weakening capability [11]. However, due to the asymmetric field distribution in CPPMMs [12], torque pulsation is even more than the fractional slot surface-mounted PM machines [13]. Therefore, studying of torque pulsation (due to the PM and armature current interaction including the main and the other higher-order harmonics), as the main source of torque ripple in CPPMMs is an important and interesting issue.

To study the performance of CPPMMs, numerical [9] and analytical [14,15] models are presented for computation of the air gap flux density. However, the torque ripple is not studied in these pieces of literature. To reduce the pulsating electromagnetic torque some literature proposed using armature current waveform shaping in the time-domain [16-18]. However, they require advanced drive controllers and a high computational burden. To simplify the required current controller and reduce the computational burden, harmonic-domain based methods [19-21] are adopted to find the correct harmonic magnitude and phase-angle for suppressing the torque pulsation. Although the harmonic-based controller is simpler than the time-based ones, their approach is not deterministic in finding the desired current harmonics. Furthermore, they require extra hardware and computational tools for harmonic decomposition and transferring the signals between multiple reference frames. As a simple, and low-cost method, it is useful to obtain the required harmonics off-line and used them in the drive controllers, as far as the drive performance is not critical. In [22], the required harmonics are found by means of direct search method and using finite-element analysis (FEA) as the off-line computational tool. However, FEA is not as fast as the analytical models [23]. Another weakness of [23], is that there is no deterministic

S. Taghipour Boroujeni is with the Department of engineering, Shahrekord University, Shahrekord, Iran (e-mail: s.taghipour@sku.ac.ir)

S. P. Emami is with the Department of engineering, Shahrekord University, Shahrekord, Iran (e-mail: payam.em93@gmail.com).

N. Takorabet is with Université de Lorraine - GREEN, 54000 Nancy – France (e-mail: noureddine.takorabet@univ-lorraine.fr).

. A. Mahmoudi is with College of Science and Engineering, Flinders University, Australia (e-mail: amin.mahmoudi@flinders.edu.au).

approach to find the amplitude and the phase angle of the armature current harmonics.

In this paper, 2nd order current harmonic injection is proposed to suppress the torque pulsation in CPPMMs. In the proposed method, based on the machine back-emf spectrum and the main current harmonic, appropriate 2nd order harmonic of the armature current is found. In section II of the presented paper, a 2D analytical model based on subdomain analysis is provided to obtain the back-emf harmonic components. The procedure of finding the appropriate the 2nd current harmonic is described in III and the model is verified by means of FEA in IV. In IV the efficacy of the proposed 2nd order current harmonic in torque ripple minimization is investigated by comparing the torque waveforms resulted by the obtained 2nd order current harmonic and by the optimum 2nd order current harmonic which is obtained by the direct search algorithm. In the direct search algorithm, the exact waveform of the electromagnetic torque is obtained by the developed analytical model. Although the aim of the paper is not the motor drive, in this section the effect of current harmonic injection is investigated considering the rotor inertia and feeding the motor with a three-phase voltage source inverter in dynamical condition.

II. EXACT SOLUTION FOR ELECTROMAGNETIC TORQUE

The geometry of a 4-pole CPPMM is shown in Fig. 1(a). Since it is aimed to compute only the electromagnetic torque pulsation due to the PM and current fields interaction, the stator slots, and the resulted cogging torque are neglected. It is worth mentioning that in the fractional slot CPPMMs, the slotting effect and its resulted cogging torque are negligible. Here, since the slots are semi-closed and the ratio of the slot opening to the slot pitch is too small (usually in fractional-slot machines), the Carter's coefficient is almost unit and the air gap length is not increased. Otherwise, the air gap must be modified by the Carter's coefficient [24]. The electromagnetic torque is found by using the Maxwell stress definition as (1) [24].

$$\begin{aligned} T_e &= \frac{r^2 L_{stk}}{\mu_0}\int_0^{2\pi} B_r B_\varphi d\varphi \\ B_r &= B_{rPM} + B_{rAR} \\ B_\varphi &= B_{\varphi PM} + B_{\varphi AR} \end{aligned} \quad (1)$$

where, B_r and B_ϕ are the resultant radial and circumferential components due to the PMs and the armature currents. The subscripts PM and AR in (1) denote the PMs and the armature current, respectively. Hereafter, the PMs and armature flux density are found by means of subdomain analysis [25].

A. Flux density of the PMs

The subdomain technique is used to obtain the no-load magnetic flux density in Fig. 1(b). Due to the symmetry in the distribution of the PMs flux density, only two regions are considered. The geometry of these regions and their dominant equations are given in (2) and (3), respectively.

$$\text{No. I:} \quad -\frac{\pi}{p} < \varphi < \frac{\pi}{p} \quad \text{and} \quad R_m < r < R_s \quad (2)$$

$$\text{No. II:} \; -\frac{\alpha_r \pi}{2p} < \varphi < \frac{\alpha_r \pi}{2p} \; \text{and} \; R_r < r < R_m$$

$$\begin{aligned} \nabla^2 A_I &= 0 \\ \nabla^2 A_{II} &= -\mu_0 \nabla \times M \end{aligned} \quad (3)$$

where, α_r, R_s, R_r, and R_m are given in Fig. 1, p is the number of the machine pole pairs and M is the PM magnetization vector which is considered in the radial direction. There is even-symmetry in the radial flux density in the machine air gap and the vector magnetic field in region I yields as (4).

$$A_I = \sum_{\upsilon=1,2,\ldots} (a_\upsilon r^{-\upsilon p} + b_\upsilon r^{\upsilon p}) \sin \upsilon p \varphi \quad (4)$$

To satisfy the boundary condition at $r=R_s$ (zero circumferential field), b_υ should be considered as (5).

$$b_\upsilon = a_\upsilon R_s^{-2\upsilon p} \quad (5)$$

In addition, there is zero tangential flux density at the lateral borders of the rotor slots ($\phi = \pm\alpha_r\pi/2p$) as well as the odd symmetry in the circumferential flux density distribution the rotor slot region. Therefore, the general solution of the magnetic potential vector inside the rotor slot is expressed as given in (6).

$$A_{II} = \sum_n (c_n r^{-\frac{np}{\alpha_r}} + d_n r^{\frac{np}{\alpha_r}} + K_n r) \sin \frac{np}{\alpha_r} \varphi \quad (6)$$

where, K_n is the particular solution and given in (7), B_{rem} is the PM remanence and α_p determines the PM arc (Fig. 1).

$$K_n = \frac{4 B_{rem} \alpha_r^2}{\mu_0 n\pi \left(\alpha_r^2 - (n\pi)^2\right)} \sin\left(\frac{n\pi}{2}\frac{\alpha_p}{\alpha_r}\right) \quad (7)$$

To satisfy the boundary condition (zero circumferential field) at $r=R_r$ in the rotor slot regions, d_n must equal as (8).

$$d_n = c_n R_r^{-\frac{2np}{\alpha_r}} - K_n R_r^{-\frac{np}{\alpha_r}+1} \quad (8)$$

The unknown coefficients c_n and a_υ are obtained by considering the continuity conditions at $r=R_m$ as given in (9).

$$\left.\frac{\partial A_I}{\partial r}\right|_{r=R_m} = \left.\frac{\partial A_{II}}{\partial r}\right|_{r=R_m} \quad (9)$$

$$\left.\frac{\partial A_I}{\partial \varphi}\right|_{r=R_m} = \left.\frac{\partial A_{II}}{\partial \varphi}\right|_{r=R_m}$$

Applying the correlation technique [11] on the equalities in (9), the coefficients a_υ and c_n are obtained as (10).

$$\begin{bmatrix}\mathbf{c}\\ \mathbf{a}\end{bmatrix} = \begin{bmatrix}\mathbf{D} & \mathbf{E}\\ \mathbf{F} & \mathbf{G}\end{bmatrix}^{-1}\begin{bmatrix}\mathbf{H}\\ \mathbf{L}\end{bmatrix} \quad (10)$$

where **c** and **a** include N_{max} and V_{max} number of the harmonics of c_n and a_υ, respectively, **D** and **G** are diagonal matrixes. The element of (10) are reported in (11), where the functions $S(n,\upsilon)$ and $T(n,\upsilon)$ are given in (12).

Computing the filed coefficients from (10), (5), (7), and (8), the PM flux density components in the air gap yield as (13). The obtained field components in (13) will be used later for calculating the back-emf and the electromagnetic torque.

$$D_{n,n} = \frac{n\pi}{2\alpha_r}\left(R_m^{-\frac{np}{\alpha_r}} + R_r^{-\frac{2np}{\alpha_r}} R_m^{\frac{np}{\alpha_r}}\right)$$

$$E_{n,\upsilon} = -\upsilon p\left(R_m^{-\upsilon p} + R_s^{-2\upsilon p} R_m^{\upsilon p}\right) S(n,\upsilon)$$

$$H_{n,1} = \frac{n\pi}{2\alpha_r} K_n\left(R_m^{\frac{np}{\alpha_r}} R_r^{-\frac{np}{\alpha_r}+1} - R_m\right) \quad (11)$$

$$L_{\upsilon,1} = K_n\left(\frac{np}{\alpha_r} R_m^{\frac{np}{\alpha_r}-1} R_r^{-\frac{np}{\alpha_r}+1} - 1\right) T(\upsilon,n)$$

$$F_{\upsilon,n} = \frac{np}{\alpha_r}\left(R_m^{\frac{np}{\alpha_r}-1} R_r^{-\frac{2np}{\alpha_r}} - R_m^{-\frac{np}{\alpha_r}-1}\right) T(\upsilon,n)$$

$$G_{\upsilon,\upsilon} = \frac{1}{2}\upsilon p\left(R_m^{-\upsilon p-1} - R_s^{-2\upsilon p} R_m^{\upsilon p-1}\right)$$

$$S(n,\upsilon) = \int_{-\frac{\alpha_r}{2}}^{\frac{\alpha_r}{2}} \cos(\upsilon p\varphi)\cos(\frac{np}{\alpha_r}\varphi) d\varphi \quad (12)$$

$$T(\upsilon,n) = \int_{-\frac{\alpha_r}{2}}^{\frac{\alpha_r}{2}} \sin(\upsilon p\varphi)\sin(\frac{np}{\alpha_r}\varphi) d\varphi$$

$$B_{rPM} = -\frac{1}{r}\frac{\partial A_I}{\partial \varphi} = -\sum_\upsilon \frac{\upsilon p}{r}(a_\upsilon r^{-\upsilon p} + b_\upsilon r^{\upsilon p})\cos\upsilon p\varphi \quad (13)$$

$$B_{\varphi PM} = \frac{\partial A_I}{\partial r} = \sum_\upsilon \frac{\upsilon p}{r}(b_\upsilon r^{\upsilon p} - a_\upsilon r^{-\upsilon p})\sin\upsilon p\varphi$$

B. Armature flux density

To obtain the armature flux density, the air gap region is divided into p+1 regions as given in (14). The governing equations on all regions are in the Laplace form.

No. I: $R_m < r < R_s$ (14)

No. i : (i=2,3,...,p+1)

$$\frac{\pi}{p}(i-2-\alpha_r) < \varphi < \frac{\pi}{p}(i-2+\alpha_r) \text{ and } R_r < r < R_m$$

The general solution of the armature vector magnetic field in region I yields as (15).

$$A_I = \sum_\upsilon \begin{pmatrix}(a_{c\upsilon} r^{-\upsilon} + b_{c\upsilon} r^{\upsilon})\cos\upsilon\varphi +\\ (a_{s\upsilon} r^{-\upsilon} + b_{s\upsilon} r^{\upsilon})\sin\upsilon\varphi\end{pmatrix} \quad (15)$$

To satisfy the boundary condition at $r=R_s$ ($B_\phi=\mu_0 J(\phi)$), $b_{s\upsilon}$ and $b_{c\upsilon}$ should be considered as (16). where $J_{s\upsilon}$ and $J_{c\upsilon}$ are the armature Fourier coefficients as given in (17).

$$b_{c\upsilon} = -\frac{\mu_0 J_{c\upsilon}}{\upsilon R_s^{\upsilon-1}} + a_{c\upsilon} R_s^{-2\upsilon} \quad (16)$$

$$b_{s\upsilon} = -\frac{\mu_0 J_{s\upsilon}}{\upsilon R_s^{\upsilon-1}} + a_{s\upsilon} R_s^{-2\upsilon}$$

$$J_{AR}(\varphi)=\sum_{\upsilon}J_{c\upsilon}\cos\upsilon\varphi+J_{s\upsilon}\sin\upsilon\varphi \tag{17}$$

In addition, there is zero tangential flux density at the lateral borders of the rotor slots ($\phi=\pm\alpha_r\pi/2p$). Therefore, the general solution of the magnetic potential vector in this region is expressed as given in (18).

$$A_{II}=\sum_{n}(c_n r^{-\frac{np}{\alpha_r}}+d_n r^{\frac{np}{\alpha_r}})\sin\frac{np}{\alpha_r}\varphi \tag{18}$$

To satisfy the boundary condition (zero circumferential field) at $r=R_r$ in the rotor slot regions, d_n must equal as (19).

$$d_n=c_n R_r^{-\frac{2np}{\alpha_r}} \tag{19}$$

The unknown coefficients c_n and a_υ are obtained by considering the continuity conditions at $r=R_m$ (see (20) and (21)) and using the correlation technique. The coefficients a_υ and c_n are obtained as (22)

$$\left.\frac{\partial A_I}{\partial r}\right|_{r=R_m}=\left.\frac{\partial A_{II}}{\partial r}\right|_{r=R_m} \tag{20}$$

$$\left.\frac{\partial A_I}{\partial \varphi}\right|_{r=R_m}=\left.\frac{\partial A_{II}}{\partial \varphi}\right|_{r=R_m} \tag{21}$$

$$\begin{bmatrix}\mathbf{a_c}\\ \mathbf{a_s}\\ \mathbf{c_1}\\ \vdots\\ \mathbf{c_P}\end{bmatrix}=\begin{bmatrix}\mathbf{D} & \mathbf{0} & \mathbf{E_{c1}} & \dots & \mathbf{E_{cP}}\\ \mathbf{0} & \mathbf{D} & \mathbf{E_{s1}} & \dots & \mathbf{E_{sP}}\\ \mathbf{X_{c1}} & \mathbf{X_{s1}} & \mathbf{G_1} & \dots & \mathbf{0}\\ \vdots & \vdots & \vdots & \dots & \vdots\\ \mathbf{X_{sP}} & \mathbf{X_{sP}} & \mathbf{0} & \dots & \mathbf{G_P}\end{bmatrix}^{-1}\begin{bmatrix}\mathbf{H_c}\\ \mathbf{H_s}\\ \mathbf{L_1}\\ \vdots\\ \mathbf{L_P}\end{bmatrix} \tag{22}$$

where $\mathbf{a_c}$ and $\mathbf{a_s}$ include V_{max} number of harmonics for $a_{c\upsilon}$ and $a_{s\upsilon}$, $\mathbf{c_i}$ include N_{max} number of harmonics for c_{in}, and $\mathbf{D_c}$, $\mathbf{D_s}$, and $\mathbf{G_i}$ are diagonal matrixes. The element of (22) are reported in (23), where the functions $S_i(n,\upsilon)$ and $T_i(n,\upsilon)$ are given in (24).

$$D_{\upsilon,\upsilon}=\frac{\upsilon}{2}\left(R_s^{-2\upsilon}R_m^{\upsilon-1}-R_m^{-\upsilon-1}\right)$$

$$\left(H_{c\ \upsilon,1},H_{s\ \upsilon,1}\right)=\frac{\mu_0}{2}R_m^{\upsilon-1}R_s^{-\upsilon+1}\left(J_{c\upsilon},J_{s\upsilon}\right)$$

$$L_{i\ \upsilon,1}=-\frac{\mu_0}{2}R_m^{\upsilon}R_s^{-\upsilon+1}\left(J_{c\upsilon}S_i(\upsilon,n)+J_{s\upsilon}V_i(\upsilon,n)\right)$$

$$E_{ci\ \upsilon,n}=\frac{np}{\alpha_r}\left(R_m^{\frac{np}{\alpha_r}-1}R_r^{-\frac{2np}{\alpha_r}}-R_m^{\frac{np}{\alpha_r}-1}\right)U_i(\upsilon,n)$$

$$E_{si\ \upsilon,n}=\frac{np}{\alpha_r}\left(R_m^{\frac{np}{\alpha_r}-1}R_r^{-\frac{2np}{\alpha_r}}-R_m^{\frac{np}{\alpha_r}-1}\right)T_i(\upsilon,n)$$

$$G_{i\ \upsilon,\upsilon}=\frac{np}{2\alpha_r}\left(R_m^{-\frac{np}{\alpha_r}}-R_r^{-2\frac{np}{\alpha_r}}R_m^{\frac{np}{\alpha_r}}\right)$$

$$X_{ic\ n,\upsilon}=\upsilon\left(R_m^{-\upsilon}+R_m^{\upsilon}R_s^{-2\upsilon}\right)S_i(\upsilon,n)$$

$$X_{is\ n,\upsilon}=\upsilon\left(R_m^{-\upsilon}+R_m^{\upsilon}R_s^{-2\upsilon}\right)V_i(\upsilon,n) \tag{23}$$

$$S_i(n,\upsilon)=\int_{-\frac{\pi}{p}(i-2-\alpha_r)}^{\frac{\pi}{p}(i-2+\alpha_r)}\cos(\upsilon\varphi)\cos(\frac{np}{\alpha_r}\varphi)d\varphi$$

$$T_i(\upsilon,n)=\int_{-\frac{\pi}{p}(i-2-\alpha_r)}^{\frac{\pi}{p}(i-2+\alpha_r)}\sin(\upsilon\varphi)\sin(\frac{np}{\alpha_r}\varphi)d\varphi \tag{24}$$

$$U_i(n,\upsilon)=\int_{-\frac{\pi}{p}(i-2-\alpha_r)}^{\frac{\pi}{p}(i-2+\alpha_r)}\cos(\upsilon\varphi)\sin(\frac{np}{\alpha_r}\varphi)d\varphi$$

$$V_i(\upsilon,n)=\int_{-\frac{\pi}{p}(i-2-\alpha_r)}^{\frac{\pi}{p}(i-2+\alpha_r)}\sin(\upsilon\varphi)\cos(\frac{np}{\alpha_r}\varphi)d\varphi$$

Knowing the coefficients in (22), (16) and (19), the armature field components yield as (25).

$$B_{rAR} = -\frac{1}{r}\frac{\partial A_I}{\partial \varphi} = \sum_{\upsilon}\frac{\upsilon}{r}\begin{pmatrix}(a_{c\upsilon}r^{-\upsilon}+b_{c\upsilon}r^{\upsilon})\sin\upsilon\varphi-\\(a_{s\upsilon}r^{-\upsilon}+b_{s\upsilon}r^{\upsilon})\cos\upsilon\varphi\end{pmatrix} \quad (25)$$

$$B_{\varphi AR} = \frac{\partial A_I}{\partial r} = \sum_{\upsilon}\frac{\upsilon}{r}\begin{pmatrix}(b_{c\upsilon}r^{\upsilon}-a_{c\upsilon}r^{-\upsilon})\cos\upsilon\varphi+\\(b_{s\upsilon}r^{\upsilon}-a_{s\upsilon}r^{-\upsilon})\sin\upsilon\varphi\end{pmatrix}$$

III. FINDING APPROPRIATE ARMATURE CURRENT HARMONICS

Injecting appropriate current harmonics is a well-known technique to suppress the torque ripple. Knowing the obtained field components in (13) and (25), the torque could be exactly predicted by (1) even in the presence of armature current harmonics. Since analytical models are fast, (1) could be used in a direct search algorithm to evaluate and find the minimum torque ripple as carried out in IV. However, it is not applicable to use (1) and find the appropriate current harmonic directly before computing the Maxwell integral. In other words, the explicit influence of the armature current harmonics on the torque pulsation is not clear in (1). As a simple and approximate approach, the machine torque could be obtained by (26) [23].

$$T_e(t) = \sum_{x\in\{a,b,c\}}\frac{e_x(t)i_x(t)}{\omega_r} \quad (26)$$

where, e_x and i_x are the back-emf and the current of phase x, and ω_r is the rotor mechanical speed. In (26), the effect of the air gap saliency is not considered. Since the PM torque is much higher than the reluctance torque, (26) could be used to estimate approximate values of the torque harmonics. Back-emf is the derivative of the no-load flux linkage as given in (27), where, λ_{PMx} is the no-load flux linkage of phase x, and L_{stk} is the machine stack-length.

$$e_x(t) = \frac{d}{dt}\lambda_{PMx}(t) = \omega_r\frac{d}{d\theta_r}\lambda_{PMx}(t) \quad (27)$$

$$\lambda_{PMx} = R_s L_{stk}\int_{\gamma_{xi}} B_{rPM}(\varphi,\theta_r)d\varphi$$

It is useful to express the current and back-emf in the Fourier form as given in (28).

$$\begin{aligned} e_x(t) &= \sum E_i\cos(i\omega t+\psi_i)\\ i_x(t) &= \sum I_i\cos(i\omega t+\varphi_i)\end{aligned} \quad (28)$$

where, E_i and I_i are the magnitude and φ_i and ψ_i are the corresponding phase angles of the ith harmonic in the back-emf and current waveforms, respectively. Using the Fourier forms of the current and back-emf in (28) inside (26), it is obvious that the same-order harmonics in phases back-emf and current will result in DC electromagnetic torque and non-equal order harmonics generate electromagnetic torque pulsations. Higher harmonics amplitude of the non-equal order current and back-emf harmonics result in higher torque pulsation.

The interaction of the m^{th} harmonic of the back-emf with the n^{th} harmonic of the current ($m\neq n$) in phase "a" of the machine results in torque pulsation with frequencies of $(m\pm n)\omega$ as given in (29), where the superscript "a" denotes the contribution of phase "a" in producing torque pulsation. The resultant torque pulsation for all phases are reported in (30), where q_{cn} is the current phase sequence for the n^{th} harmonic, q_{vm} is the back-emf phase sequence for the m^{th} harmonic and i={0,1,2} are linked with phases {a,b,c}, respectively. The positive, negative, and zero phase sequences are considered as +1, -1 and 0, respectively. Using (30), the resultant electromagnetic torque pulsation for different combinations of the phase sequences of the current and back-emf are given in (31), respectively.

$$\begin{aligned} T^{a}_{r(n,m)} &= \frac{E_m I_n}{\omega_r}\sin(n\omega t+\varphi_n)\sin(m\omega t+\psi_m)\\ &= \frac{E_m I_n}{2\omega_r}\cos((m-n)\omega t+\psi_m-\varphi_n)\\ &-\frac{E_m I_n}{2\omega_r}\cos((m+n)\omega t+\psi_m+\varphi_n)\end{aligned} \quad (29)$$

$$\begin{aligned} T_{r(n,m)} &= \sum_{i=\{0,1,2\}} T^{i}_{r(n,m)} =\\ &\frac{E_m I_n}{\omega_r}\sum_{i=\{0,1,2\}}\begin{bmatrix}\sin\left(n\omega t+\varphi_n+\frac{2\pi i q_{cn}}{3}\right)\times\\ \sin\left(m\omega t+\psi_m+\frac{2\pi i q_{vm}}{3}\right)\end{bmatrix}\end{aligned} \quad (30)$$

$$T_{r(n,m)} = \begin{cases} \frac{3E_m I_n}{2\omega_r}\cos\left((m-n)\omega t + \psi_m - \varphi_n\right) & q_{vm}.q_{cn} = 1 \\ -\frac{3E_m I_n}{2\omega_r}\cos\left((m+n)\omega t + \psi_m + \varphi_n\right) & q_{vm}.q_{cn} = -1 \\ 0 & q_{vm} \text{ or } q_{cn} = 0 \\ \frac{3E_m I_n}{2\omega_r}\begin{bmatrix}\cos\left((m-n)\omega t + \psi_m - \varphi_n\right) \\ -\cos\left((m+n)\omega t + \psi_m + \varphi_n\right)\end{bmatrix} & q_{vm} = q_{cn} = 0 \end{cases} \quad (31)$$

As well as, the pulsating torque due to the interaction of m^{th} and n^{th} harmonic orders in the back-emf and current, i.e., $T_r(n,m)$, there is another torque pulsation component with frequency of $(m+n)\omega$ or $(m-n)\omega$ which is the result of the interaction between the n^{th} and m^{th} harmonic orders in the back-emf and current, i.e., $T_r(m,n)$. Therefore, to suppress the electromagnetic torque pulsation with the same frequency, the resultant toque pulsation $T_{r(m,n)}+T_{r(n,m)}$ must be zero.

Since it is not possible to eliminate the influence of all harmonics in back-emf, the most dominant and important one, i.e., the 2nd order harmonic is planned to be compensated by injecting the 2nd order harmonic in the armature current in the considered CPPMM. Since the 2nd harmonics in the back-emf has the negative phase sequence, the injected 2nd harmonic of the current must have the negative phase sequence too.

Based on (31), the resulted torque harmonics due to the interaction of the five first harmonics of the back-emf and 1st and 2nd armature current harmonics are given in Table 1. It is worth mentioning that the low order harmonics have higher magnitude and result in higher torque pulsation. As highlighted in Table 1, the 3p harmonic order in the electromagnetic torque is the result of the 1st harmonic of the current with the 2nd and 4th harmonics in the back-emf voltage. In comparison with the 4th harmonic component of the back-emf, the 2nd one has a higher magnitude and produces a higher 3p order toque harmonic than the 4th one. In addition, the interaction of the 2nd order harmonic with the 1st and 5th back-emf components produces 3p harmonic order in the electromagnetic torque. However, the 1st harmonic component is greater than the 5th one in the back-emf, and results in a higher 3p order toque harmonic. Therefore, $T_{r(2,1)}$ is used to nullify $T_{r(1,2)}$. To nullify only $T_{r(1,2)}$, the 2nd order harmonic magnitude and the phase angle is obtained considering $T_{r(1,2)}=-T_{r(1,2)}$ as given in (32).

$$I_2 = \frac{E_2 I_1}{E_1} \quad (32)$$
$$\varphi_2 = \pi + \varphi_1 + \psi_2 - \psi_1$$

IV. Results

A. Model verification

A CPPMM with 6-slot/4-pole CPPMM is considered as the case study (see Fig. 1 (a)). The data of the considered machine is given in Table 2. To investigate the validity of the provided model FEA simulations are carried out. Hereafter, the values of α_r and α_p are considered the same in all designs ($\alpha_p=\alpha_r$) to use the maximum available space of the rotor slots and increase the PM flux linkage. The no-load flux density components of the CPPMMs for α_r=0.65 are obtained by means of FEA and the proposed model in Fig. 2 (a) and (b). The distribution of the field density, the used meshes and the B-H curves of the used material (M19) is illustrated in Fig.2 (c)-(e), respectively. It is seen that the proposed model is in good consistency with FEA. It is worth mentioning that, the limited number of the used frequencies in the Fourier series caused some fluctuations in the curves in Fig.2. Considering a higher number of frequencies will reduce the fluctuation but increase the computational burden.

The harmonic spectrum of the PM flux linkage (λ_{PM}) is given in Fig. 3 for different values of α_r. As seen in Fig. 3, the highest magnitudes for the working (first PM harmonic) are obtained with α_r =0.7 and α_r =0.75. However, in these cases, the rotor teeth flux density goes beyond the considered saturation limit (1.5T). To maximizing the 1st harmonic of the PM flux linkage while respecting the saturation constrain, α_r is selected as 0.6 and α_r =0.65. However, in comparison with α_r =0.5, in the machines with α_r=0.6 and α_r=0.65, there are considerable 2nd order harmonic components (2p=4) in the back-emf and the PM flux linkage.

The magnitude and phase-angle spectrums for the considered CPPMMs at speed of ω_r=20 rad./sec. are given in Figs. 4(a) and (b), respectively. As seen in Fig. 4(a) there is considerable 2nd harmonic component (2p=4) in the back-emf of the machines with α_r=0.65 and α_r=0.65, while the 5th-order (5p=10) harmonic in the machine with α_r=0.5 is also significant. The back-emf harmonic components result in torque pulsation. The torque waveforms for the considered CPPMMs excited with three-phase balanced and synchronized ($f=\omega p/2/\pi$) current $I_1=1\angle-30^o$ are obtained by the proposed model and FEA as illustrated in Fig.5. As seen there is a good consistency between the FEA and analytical model results. In addition, as expected the torque pulsation and the average torque increase by increasing the PM arc.

B. Approach Efficacy

To investigate the efficacy of the proposed method in torque ripple minimization, the obtained torque waveform by the proposed method is compared by the one obtained by injecting the best solution for the 2nd order current harmonic. The best

solution for the 2nd order current harmonic is obtained by applying a direct search algorithm. In the direct search algorithm, the variation of the magnitude and the phase angle of the 2nd order harmonic is in the step of 0.05A for 0 to 0.7A and 2° for 0 to 358°, respectively. The developed analytical model in III is used in the direct search algorithm for the torque waveform computation.

The obtained torque pulsation by using (32) and the direct search method, for the CPPMM with α_r=0.6 and two armature currents with different 1st order current harmonics (I_1=1∠-30° and I_1=1∠0°) are given in Fig. 6. The electromagnetic torque waveforms obtained by injecting the 2nd order harmonic current found by (32) and the direct search method for the mentioned conditions are given in Fig. 7.

As seen in Fig.6 the proposed 2nd order current harmonic from (32) is very close the best ones obtained by the direct search algorithm. From Fig.7 it is observable that torque pulsation is decreased by injecting 2nd order current harmonic obtained by (32), but not as much as decreased by injecting the best 2nd order current harmonic obtained by the direct search algorithm. Although the proposed method is not as effective as the direct search method, it is efficient enough considering its negligible computation burden over the direct search method. Because, in the direct search algorithm, the torque pulsation must be computed for all possible 2nd current harmonic solutions (more than 2500 candidates), that is a time-consuming task, while in the proposed approach in III the 2nd current harmonic is obtained directly by (32). Therefore, considering the fast response of the proposed method for finding the desired 2nd order harmonic current, its precision is acceptable as the initial solution for finding the best solution by applying a local search algorithm especially in the on-line working condition.

The reason that (32) cannot reduce the torque pulsation more, is that the effect of higher harmonic components in the torque pulsation is neglected in (32) (e.g., $T_{r(1,4)}$ and $T_{r(2,6)}$). In addition, the effect of magnetic saliency is neglected in (32). Due to the mentioned reasons the dominant harmonic ($3p=6$) of the electromagnetic torque by using (32) is not nullified completely (see Fig. 8). The merit of the proposed approach becomes notable when the machine model is not exactly known due to saturation or other parameter variation. In this case, the best solution could be found by using iterative local search methods and the proposed solution in (32) could serve as a good initial solution that reduces the computation time of the optimization algorithm. In other words, due to inaccuracies, the predicted 2nd order harmonic is not exactly the best one. For this reason, some paper proposed to find the best 2nd order harmonics by means of on-line optimization algorithms in each working condition. Therefore, to decrease the computational burden of such algorithms, using the proposed method is very useful to find a good initial solution in each working condition. To consider the effect of saturation, the torque curves in two cases is obtained in nonlinear magnetic condition and are illustrated in Fig.9.

C. Dynamic Simulations

Although the aim of the paper is not the motor drive, in this section the effect of the current harmonic injection is investigated by considering the rotor inertia and feeding the motor with a three-phase voltage source inverter. The used parameters are reported in Table III. Since the stator neutral point is not grounded, there are only two state variables for the flux linkages, and the related state-space equations are given in (33). The machine currents are given as functions of the flux linkages in (34). Considering λ_c=-λ_a-λ_b in (33) and adding the mechanical equations, the machine state-space equations yield (35).

$$\frac{d}{dt}\begin{pmatrix}\lambda_a-\lambda_b\\ \lambda_a-\lambda_c\end{pmatrix}=\begin{pmatrix}v_a-v_b\\ v_a-v_c\end{pmatrix}-r_s\begin{pmatrix}i_a-i_b\\ i_a-i_c\end{pmatrix} \tag{33}$$

$$\begin{pmatrix}i_a\\ i_b\end{pmatrix}=K(\theta_r)\left(\begin{pmatrix}\lambda_a\\ \lambda_b\end{pmatrix}-\begin{pmatrix}\lambda_{PMa}(\theta_r)\\ \lambda_{PMb}(\theta_r)\end{pmatrix}\right) \tag{34}$$

$$K=\begin{pmatrix}L_{aa}(\theta_r)-L_{ac}(\theta_r) & L_{ab}(\theta_r)-L_{ac}(\theta_r)\\ L_{ba}(\theta_r)-L_{bc}(\theta_r) & L_{bb}(\theta_r)-L_{bc}(\theta_r)\end{pmatrix}^{-1}$$

$$\frac{d}{dt}\begin{pmatrix}\lambda_a\\ \lambda_b\end{pmatrix}=\frac{1}{3}\begin{pmatrix}1 & 1\\ -2 & 1\end{pmatrix}\left(\begin{pmatrix}v_a-v_b\\ v_a-v_c\end{pmatrix}-r_s\begin{pmatrix}i_a-i_b\\ i_a-i_c\end{pmatrix}\right)$$

$$J\frac{d\omega}{dt}=T_e-T_L \tag{35}$$

$$\frac{d\theta_r}{dt}=\omega$$

The hysteresis switching algorithm is used for the inverter. Since the motor drive is not the scope of this study, the current controllers are not included and it is supposed the command current signals are known. In other words, the main and 2nd order harmonics of the machine currents are considered as the reference signals. The block diagram of the simulated system is given in Fig.10. In the dynamic simulation zero initial conditions are considered for the state variables except for the initial speed which is considered 20. For the condition of (α_r,I_1)=(0.6,1∠-30°), the obtained electromagnetic torque and the rotor speed with and without current harmonic injection are given in Fig.11. It is worth mentioning that the torque load are considered as the average torques reported in Fig. 7(b). Comparing the electromagnetic torque in Fig.11 (b) with the waveforms in Fig.7 (b), shows that (1) 2nd harmonic injection in the armature current could suppress the torque ripple, (2) the behavior of the torque waveform with and without current harmonic injection (in the both best and predicted optimum cases) results in the same conclusion

V. Conclusion

In this paper, 2nd order current harmonic injection is proposed to suppress the electromagnetic torque pulsation in CPPMMs. In the proposed method, appropriate 2nd order harmonic of the armature current is found. In section II of the presented paper, a 2D analytical model based on subdomain analysis is provided to obtain the required back-emf harmonic components. The model is verified by means of FEA. The efficacy of the proposed 2nd order current harmonic in torque ripple minimization is investigated by comparing the electromagnetic torque waveform resulted by the obtained 2nd order current harmonic and the torque due the optimum 2nd order current harmonic obtained by the direct search algorithm. In the direct search algorithm, the exact waveform of the electromagnetic torque is obtained by the developed analytical model. The results show that the proposed 2nd order current harmonic is close the best one obtained by the direct search algorithm (Fig. 6). The reason that the obtained 2nd order current harmonics are not the same as the best one is discussed and it is justified that the proposed method is useful to be applied due to its fastness, especially to find initial solution in the iterative online applications.

VI. Acknowledgment

This work has been financially supported by the research deputy of Shahrekord University. The grant number was 98GRD30M930.

References

[1] Taghipour-Boroujeni, S., and Zamani, V., "Influence of magnet shaping on cogging torque of surface-mounted PM machines," *Int. J. Numer. Model.*, **29**(5), pp. 859–872 (2016).
[2] Zamani, V., Taghipour-Boroujeni, S., and Takorabet N., "Optimum arrangement of PMs in surface-mounted PM machines: cogging torque and flux density harmonics," *Journal of Electrical Engineering, Springer,* **102**(3), pp. 1117–1127 (2020).
[3] Bianchi, N., Bolognani, S., Bon, D., et al , "Torque Harmonic Compensation in a Synchronous Reluctance Motor ," *IEEE Trans. Energy Convers*., **23(2)**, pp 466-473, (2008).
[4] Ashabani, M., Milimonfared, J., and Taghipour-Boroujeni, S.,"Cogging force mitigation of tubular permanent magnet machines with magnet dividing," ICEMS, Aug. 2007, Seoul South Korea, pp. 810-814
[5] Islam, R., Husain, I., Fardoun, A., et al "Permanent magnet synchronous motor magnet designs with skewing for torque ripple and cogging torque reduction," *IEEE Trans. Ind. Appl.*, **45**(1), pp. 152–160 (2009).
[6] Taghipour-Boroujeni, S., Takorabet, N., Mezani, S., et al, "Using and enhancing the cogging torque of PM machines in valve positioning applications," *IET-EPA*, **14**(12) (2020).
[7] Dajaku, G., Xie, W., and Gerling, D., "Reduction of Low Space Harmonics for the Fractional Slot Concentrated Windings Using a Novel Stator Design," *IEEE Trans. Magn.*, **50**(5), ASN: 8201012 (2014).
[8] Alberti L., and Bianchi N., "Theory and Design of Fractional–Slot Multilayer Windings*," IEEE Trans. Ind. App.,* **49**(2), pp 841-849 (2013).
[9] Chung, S. U., Kim, J. W., Chun, Y .D. , et al, "Fractional Slot Concentrated Winding PMSM With Consequent Pole Rotor for a Low-Speed Direct Drive: Reduction of Rare Earth Permanent Magnet," *IEEE Trans. Energy Convers.*, **30**(1), pp. 103–109 (2015).
[10] Chung S. U. et all., "A Novel Design of Modular Three-Phase Permanent Magnet Vernier Machine With consequent Pole Rotor," *IEEE Trans. on Magn.*, **47**(10), pp. 4215–4218 (2011).
[11] Tapia, J. A., Leonardi, F., and Lipo, T. A., "Consequent-pole permanent magnet machine with extended field-weakening capability," *IEEE Trans. Ind. Appl.*, **39(**6), pp. 1704–1709 (2003).
[12] Li, J., Wang, K., and Liu, C., "Comparative Study of Consequent-Pole and Hybrid-Pole Permanent Magnet Machines," *IEEE Trans. Energy Convers.*, **34**(2), pp. 701-711 (2019).
[13] Li, F., Wang, K., Li, J., and et al, "Electromagnetic Performance Analysis of Consequent-Pole PM Machine With Asymmetric Magnetic Pole," *IEEE Trans. Magn.*, **55**(6), ASN:8103205 (2019).
[14] Teymoori, S., Rahideh,A., Moayed-Jahromi, H., and et al, "2-D Analytical Magnetic Field Prediction for Consequent-Pole Permanent Magnet Synchronous Machines," *IEEE Trans. Magn.*, **52**(6), ASN: 8202114, (2016).
[15] Taghipour-Boroujeni, S., Emami, S. P., Takorabet, N.,, and et al "Analytical investigation of the armature current influence on the torque and radial force in eccentric consequent- pole PM machines," *IET-EPA, Wiley*, **15**(4), pp. 441-452 (2021).
[16] Flieller, D., Nguyen, N. K., Wira, P., and et al, "A self-learning solution for torque ripple reduction for non-sinusoidal permanent-magnet motor drives based on artificial neural networks," *IEEE Trans. Ind. Electron.,* **61**(2), pp.655–666, (2014).
[17] Jezernik, K., Korelic, J., and Horvat, R., "PMSM sliding mode FPGA-based control for torque ripple reduction," *IEEE Trans. Power Electron.,* **28**(7), pp. 3549–3556 (2013).
[18] Feng, G., Lai, C., and Kar, N. C., ''An Analytical Solution to Optimal Stator Current Design for PMSM Torque Ripple Minimization with Minimal Machine Losses,'' *IEEE Trans. on Ind. Elect.*, **64**(10), pp. 7655–7665, (2017).
[19] Li, L., Lee, K. M., Bai, K., and et al, "Inverse Models and Harmonics Compensation for Suppressing Torque Ripples of Multiphase Permanent Magnet Motor," *IEEE Trans. Ind. Appl.*, **65**(11), pp.8730-8739, (2018).
[20] Wu, Z., Yang, Z., Ding, K., and et al, "Order-domain-based Harmonic Injection Method for Multiple Speed Harmonics Suppression of PMSM," *IEEE Trans. Power Elec.*, **36**(4), pp. 4478-4487 (2021).
[21] Feng, G., Lai, C., and Kar, N. C., "Speed Harmonic Based Decoupled Torque Ripple Minimization Control for Permanent Magnet Synchronous Machine with Minimized Loss", *IEEE Trans. Energy Convers.*, **35**(4), pp. 1796-1805, (2020).
[22] Lee, G. H., Kim, S. I., Hong, J. P., and et al, "Torque Ripple Reduction of Interior Permanent Magnet Synchronous Motor Using Harmonic Injected Current," *IEEE Trans. Magn.*, **56**(5), pp. 1582-1585 (2008).
[23] Zarko, D., Ban, D., and Lipo, T. A., "Analytical Solution for Electromagnetic Torque in Surface Permanent-Magnet Motors Using Conformal Mapping," *IEEE Trans. Magn.*, vol. 45, no.7, July 2019, pp. 2943-2954.
[24] Taghipour-Boroujeni, S., Emami, S. P., Takorabet, N., "Fast prediction of unbalanced magnetic pull in PM machines", *Electrical Engineering*, **103**(6), pp.2595-2602 (2021).
[25] Rahideh, A., Mardaneh, M., and Korakianitis, T., "Analytical 2-D Calculations of Torque, Inductance, and Back-EMF for Brushless Slotless Machines With Surface Inset Magnets", *IEEE Trans. Magn.*, **49**(8), pp. 4873-4884 (2013).

Fig. 1. The (a) geometry and (b) variables for the considered CPPMM.

Fig. 2 (a) radial and (b) circumferential components of the PM flux density, (c) flux density distribution, (d) meshes and B-H curve of the used material in the studied machine.

Fig. 3 Harmonic spectrum of the PM flux linkage.

Fig. 4 The (a) magnitude (b) phase-angel spectrums and (c) waveforms of the studied machine back-emf at ω_r=20 rad./sec..

Fig. 5 The electromagnetic torque versus the rotor angle in mechanical degree for the CPPMM with (a) α_r=0.5, (b) α_r=0.6 and (c) α_r=0.65.

Fig.6 Torque pulsation in the case of 2nd harmonic current injection for (a) (α_r, I_1)=(0.6,1∠0) and (b) (α_r, I_1)=(0.6,1∠-30^o)

Fig. 7 Torque waveforms versus the rotor angle in mechanical degree for (a) (α_r,I_1)=(0.6,1∠0) and (b) (α_r,I_1)=(0.6,1∠-30^o).

Fig.8 Torque spectrum for (a) (α_r,I_1)=(0.6,1∠0) and (b) (α_r, I_1)=(0.6,1∠-30^o).

Fig. 9 Torque versus the rotor angle for (a) (α_r, I_1)=(0.6,1∠0) and (b) (α_r, I_1)=(0.6,1∠-30^o) in linear (L) and nonlinear (NL) magnetic cases.

Fig. 10. Block-diagram of the dynamic model of (a) the drive system, (b) the machine.

Fig. 11 Dynamic simulation results for (α_r,I_1)=(0.6,1∠-30^o) (a) Speed, (b) electromagnetic torque, and (c) currents.

TABLE I: ELECTROMAGNETIC TORQUE COMPONENTS.
TABLE II: PARAMETERS OF THE STUDIED CPPM.
TABLE III: PARAMETERS OF THE CPPM DYNAMIC SIMULATION.

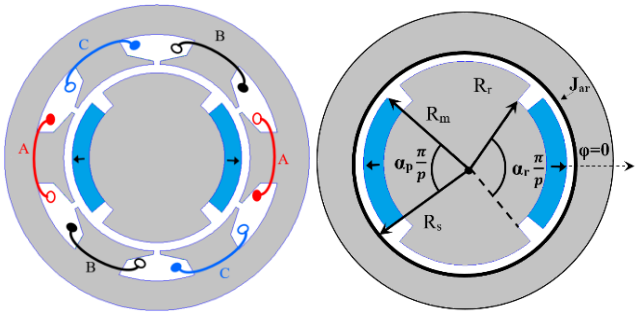

(a) *(b)*

Fig. 1. The (a) geometry and (b) variables for the considered CPPMM.

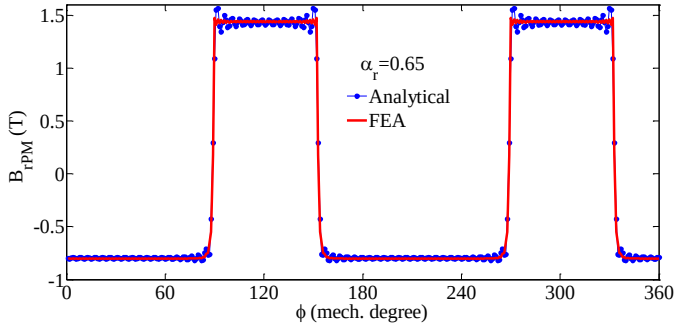

(a)

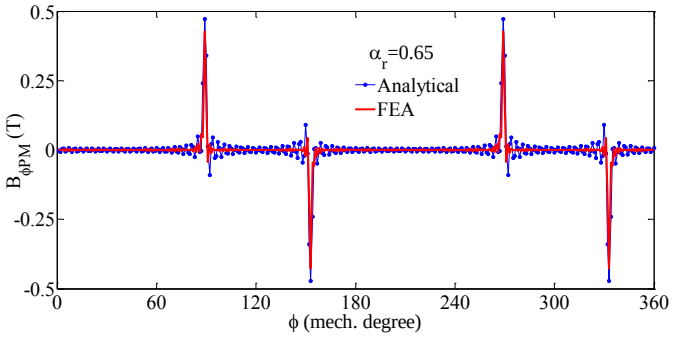

(b)

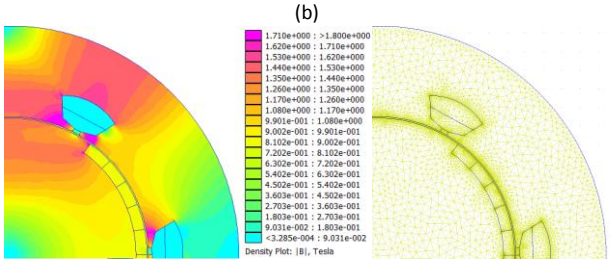

(c) (d)

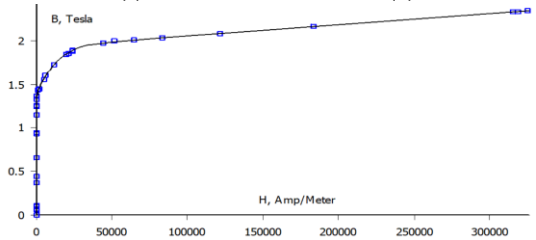

(e)

Fig. 2 (a) radial and (b) circumferential components of the PM flux density, (c) flux density distribution, (d) meshes and B-H curve of the used material in the studied machine.

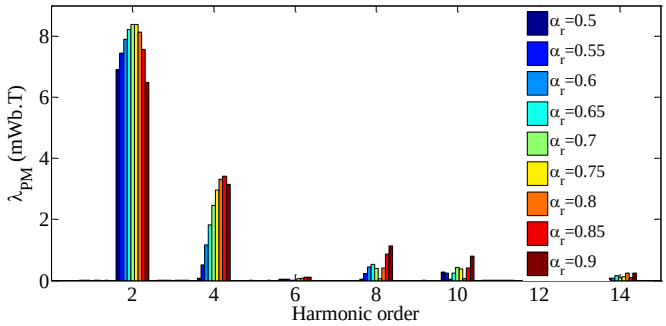

Fig. 3 Harmonic spectrum of the PM flux linkage.

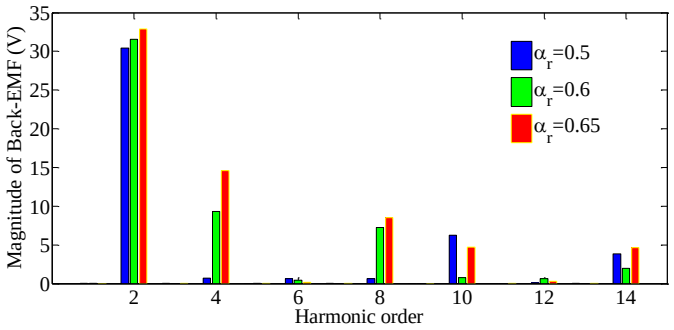

(a)

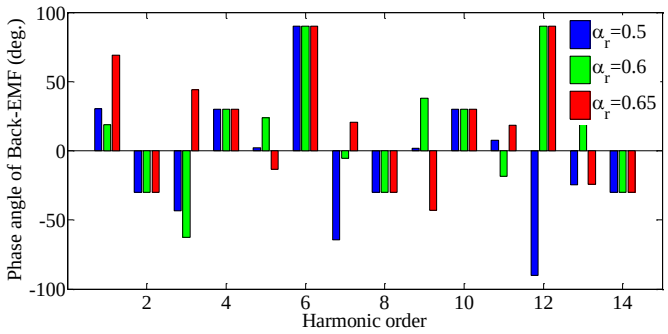

(b)

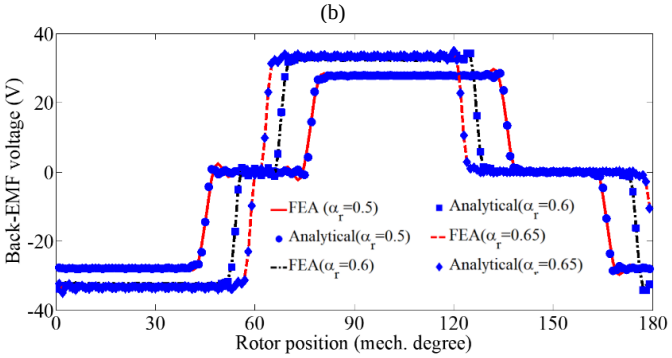

(c)

Fig. 4 The (a) magnitude (b) phase-angel spectrums and (c) waveforms of the studied machine back-emf at ω_r=20 rad./sec..

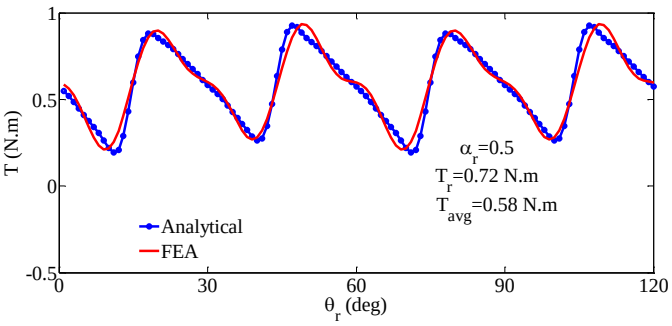

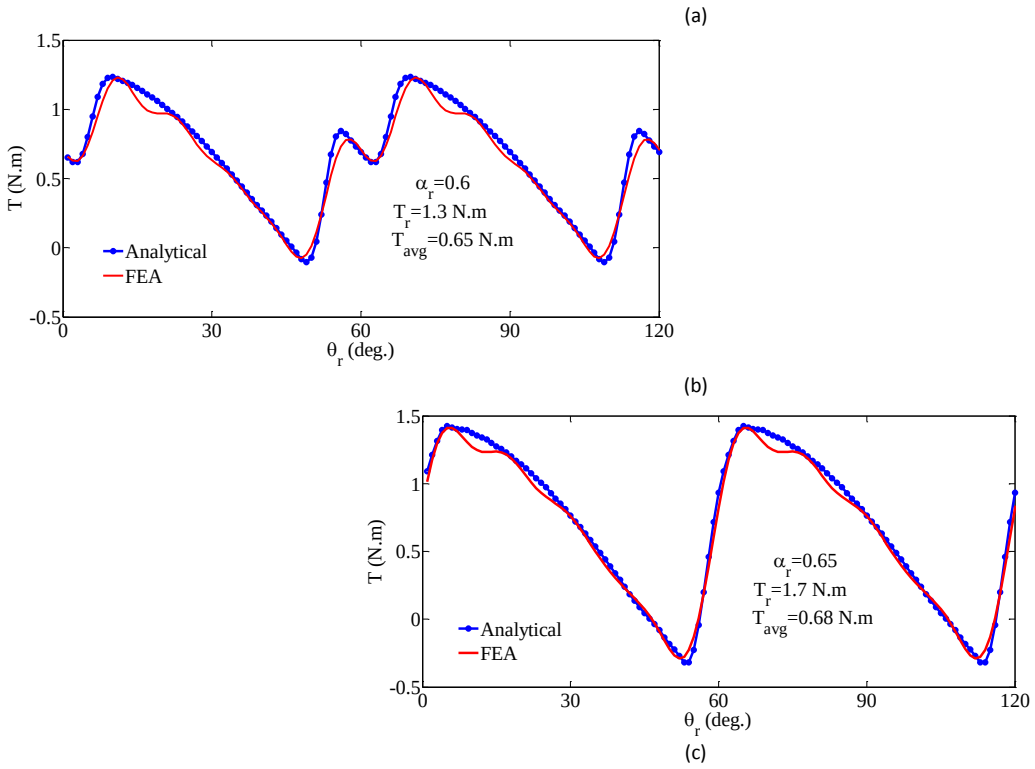

Fig. 5 The electromagnetic torque versus the rotor angle in mechanical degree for the CPPMM with (a) α_r=0.5, (b) α_r=0.6 and (c) α_r=0.65.

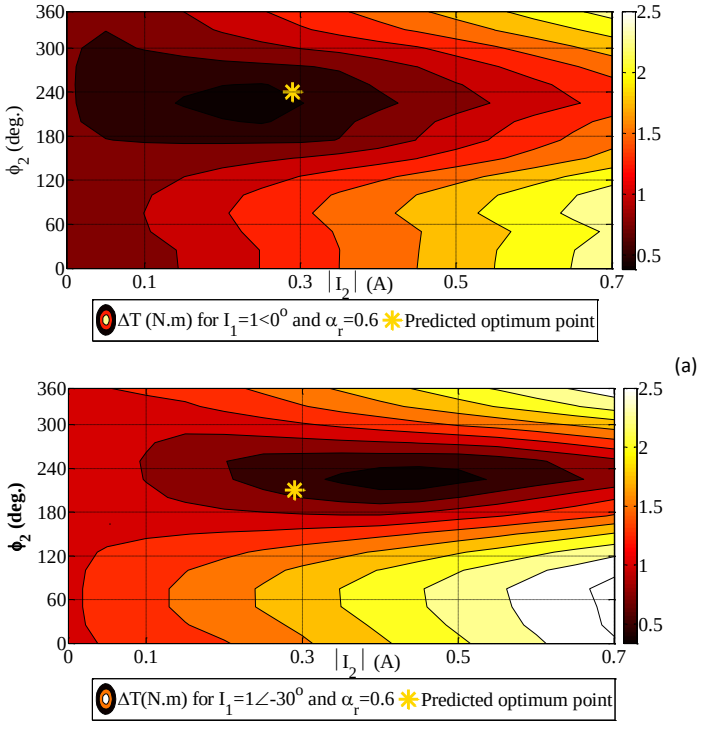

Fig.6 Torque pulsation in the case of 2nd harmonic current injection for (a) (α_r, I_1)=(0.6,1∠0) and (b) (α_r, I_1)=(0.6,1∠-30°)

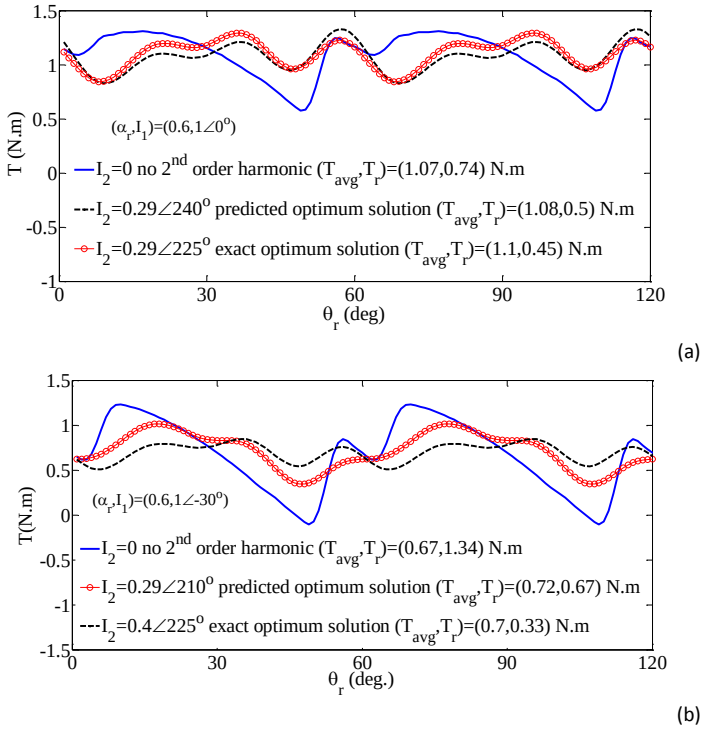

Fig. 7 Torque waveforms versus the rotor angle in mechanical degree for (a) (α_r,I_1)=(0.6,1∠0) and (b) (α_r,I_1)=(0.6,1∠-30^o).

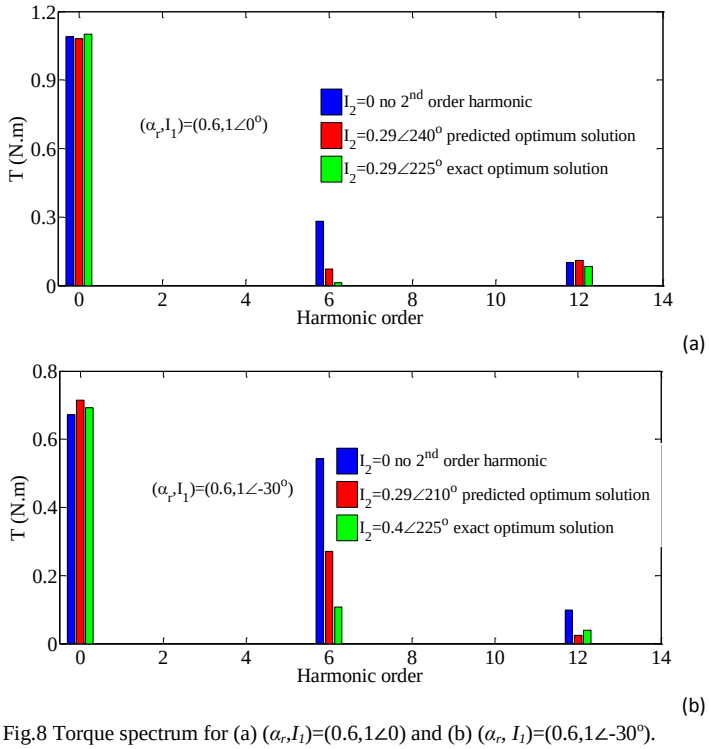

Fig.8 Torque spectrum for (a) (α_r,I_1)=(0.6,1∠0) and (b) (α_r, I_1)=(0.6,1∠-30^o).

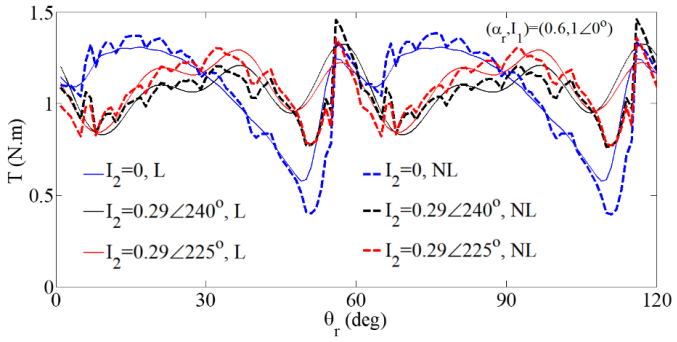

(a)

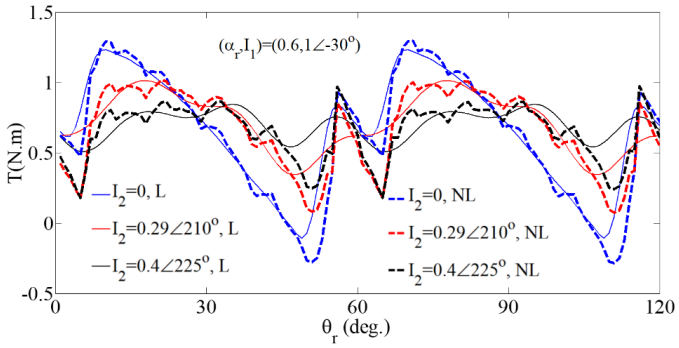

(b)

Fig. 9 Torque versus the rotor angle for (a) (α_r, I_1)=(0.6,1∠0) and (b) (α_r, I_1)=(0.6,1∠-30°) in linear (L) and nonlinear (NL) magnetic cases.

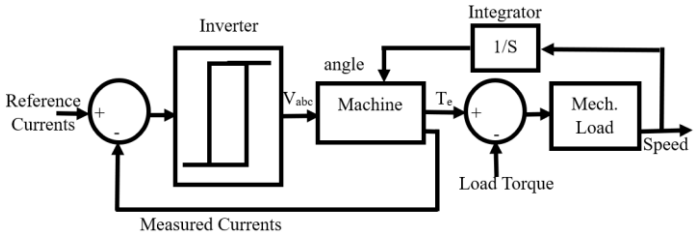

(a)

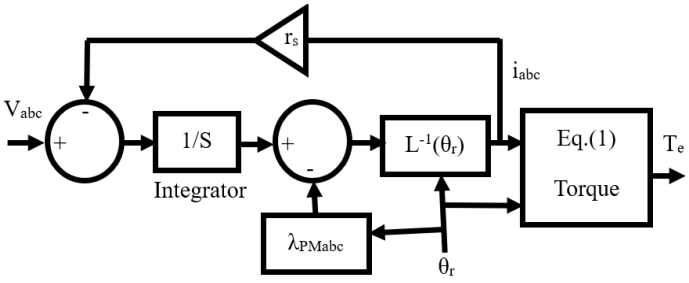

(b)

Fig. 10. Block-diagram of the dynamic model of (a) the drive system, (b) the machine.

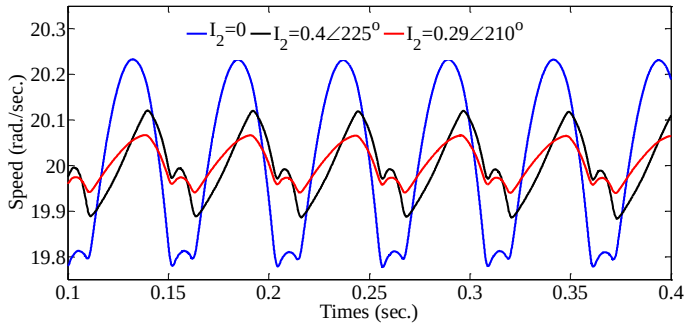

(a)

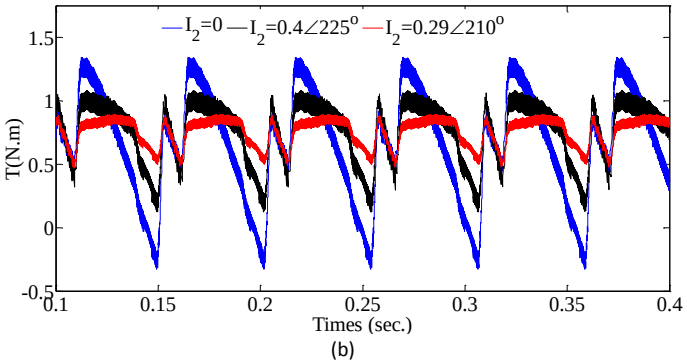

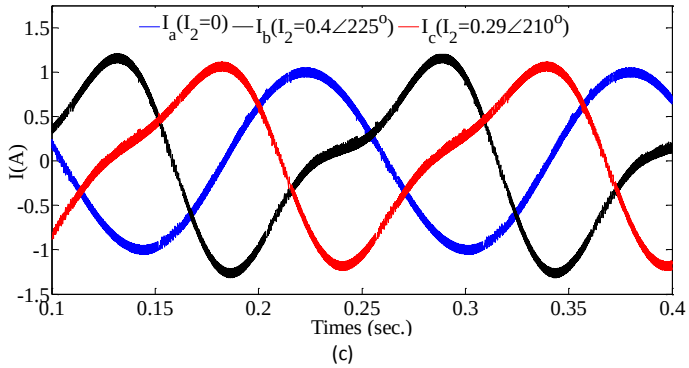

Fig. 11 Dynamic simulation results for (α_r,I_1)=(0.6,1∠-30^o) (a) Speed, (b) electromagnetic torque, and (c) currents.

TABLE I

ELECTROMAGNETIC TORQUE COMPONENTS.

Torque harmonic components		Back-emf (harmonic, q_{vm})				
		(p,+)	($2p$,-)	($3p$,0)	($4p$,+)	($5p$,-)
current (harmonic, q_{cn})	(p,+)	0	$3p$	---	$3p$	$6p$
	($2p$,-)	$3p$	0	---	6p	$3p$

TABLE II

PARAMETERS OF THE STUDIED CPPM.

Parameter	Symbol	Value
Pole pairs	p	2
Number of slots	Q_s	6
No. turn per phase	N	200
Rotor radius	R_r	68.3 mm
Magnet radius	R_m	74.3 mm
Air gap length	g	0.7 mm
Inner stator radius	R_s	75.0 mm
Stack length	L_{stk}	50.0 mm
PM remanence	B_{rem}	1.2T

TABLE III

PARAMETERS OF THE CPPM DYNAMIC SIMULATION.

Parameter	Symbol	Value
Stator resistance	r_s	0.1 Ω
DC link voltage	V_{DC}	70 V
Rotor inertia	J	0.002 kg.m^2
Reference speed	ω^*	20 rpm

Samad Taghipour Boroujeni

Samad Taghipour Boroujeni received the B.Sc., M.Sc., and Ph.D. degrees in electrical engineering from the Department of Electrical Engineering, Amirkabir University (Tehran Polytechnic), Tehran, Iran, in 2003, 2005, and 2009, respectively. In 2008, he was a Visiting Scholar with the Electrical Engineering Department, Padova University, Padova, Italy. In 2009, he joined the Department of Engineering, Shahrekord University, Shahrekord, Iran, as an Assistant Professor, where he was serving as an Associate Professor from 2016 to 2020. He had a postdoctoral carrier in 2018-2020 in Lorrain University, Nancy, France in GREEN Lab. He has been a Full Prof. since 2020 at Shahrekord University. His research interests include modeling, design, analysis, optimization, and control of electrical machines, especially variable-speed generators.

Seyed Payam Emami

Seyed Payam Emami received the B.Sc and the M.Sc in electrical engineering from Sharekord University in 2016 and 2019 respectively. He is currently pursuing the Ph.D. degree in electrical engineering with the University of Massachusetts Lowell, MA, USA. His research interests include modeling, design, analysis, optimization, control of electrical machines, modelling and control of power electronics converters.

Noureddine Takorabet

Presently working as Professor of Electrical Engineering at Université de Lorraine, France, Prof. Noureddine TAKORABET is graduated as Engineer in Ecole Nationale Polytechnique of Algiers (Algeria). He received Master of Science from Université Henri Poincaré (Nancy-France) and PhD from Institute National Polytechnique de Lorraine in 1996 (Nancy-France). In 2019 he is chair-organizer of the 19th International Symposium on Electromagnetic Fields in Mechatronics, Electrical and Electronic Engineering ISEF2019. Actually, he is Director of the research center GREEN: Group of Research in Electrical Engineering of Nancy (20 Prof. and Ass. Prof). He is the head of international laboratory: Electrical Engineering Thai-French Research center with Kink Mongkut's University of technology North Bangkok. The main teaching activities deal with electrical machines, electromagnetics, numerical simulation and mathematics. Prof. Noureddine Takorabet advised more than 20 PhD students and published more than 80 papers in international journals and more than 150 conference papers, and some patents in collaborations with industrial partners. He led many national projects and involved in European projects H2020 about more electric aircrafts.

Amin Mahmoudi

Amin Mahmoudi (Senior Member, IEEE) received the B.Sc. degree in electrical engineering from Shiraz University, Shiraz, Iran, in 2005, the M.Sc. degree in electrical power engineering from the Amirkabir University of Technology, Tehran, Iran, in 2008, and the Ph.D. degree from the University of Malaya, Kuala Lumpur, Malaysia, in 2013. He currently works as a Lecturer with Flinders University, Adelaide, Australia. He has authored/coauthored over 150 papers in international journals and conferences. His main research interest includes where the electrical energy conversion plays a major role, such as the electrical machines and drives, renewable energy systems, and hybrid power networks. It includes the transportation electrification in which the sustainable energy efficient solutions are realized by advanced electric motors, power electronics, energy management systems and controls for electrified powertrains, and electric vehicles. He is a member of the Institution of Engineering and Technology (MIET) and a Chartered Engineer (C.Eng.). He is also a member of the Engineers Australia (MIEAust) and a Chartered Professional Engineer (C.P.Eng.).